The Soft State of Cygnus X-1 Observed With NuSTAR: A Variable Corona and a Stable Inner Disk

Walton, D. J.; Tomsick, J. A.; Madsen, K. K.; Grinberg, V.; Barret, D.; Boggs, S. E.; Christensen, Finn Erland; Clavel, M.; Craig, W. W.; Fabian, A. C.

Total number of authors:
20

Published in:
Astrophysical Journal

Link to article, DOI:
10.3847/0004-637X/826/1/87

Publication date:
2016

Document Version
Publisher's PDF, also known as Version of record

The Astrophysical Journal, 826:87 (13pp), 2016 July 20 doi:10.3847/0004-637X/826/1/87

THE SOFT STATE OF CYGNUS X-1 OBSERVED WITH *NuSTAR*: A VARIABLE CORONA AND A STABLE INNER DISK

D. J. Walton[1,2], J. A. Tomsick[3], K. K. Madsen[2], V. Grinberg[4], D. Barret[5,6], S. E. Boggs[3], F. E. Christensen[7], M. Clavel[3], W. W. Craig[3], A. C. Fabian[8], F. Fuerst[2], C. J. Hailey[9], F. A. Harrison[2], J. M. Miller[10], M. L. Parker[8], F. Rahoui[11,12], D. Stern[1], L. Tao[2], J. Wilms[13], and W. Zhang[14]

[1] Jet Propulsion Laboratory, California Institute of Technology, Pasadena, CA 91109, USA
[2] Space Radiation Laboratory, California Institute of Technology, Pasadena, CA 91125, USA
[3] Space Sciences Laboratory, University of California, Berkeley, CA 94720, USA
[4] MIT Kavli Institute for Astrophysics and Space Research, MIT, 70 Vassar Street, Cambridge, MA 02139, USA
[5] Universite de Toulouse, UPS-OMP, IRAP, Toulouse, France
[6] CNRS, IRAP, 9 Av. colonel Roche, BP 44346, F-31028 Toulouse cedex 4, France
[7] DTU Space, National Space Institute, Technical University of Denmark, Elektrovej 327, DK-2800 Lyngby, Denmark
[8] Institute of Astronomy, University of Cambridge, Madingley Road, Cambridge CB3 0HA, UK
[9] Columbia Astrophysics Laboratory, Columbia University, New York, NY 10027, USA
[10] Department of Astronomy, University of Michigan, 1085 S. University Avenue, Ann Arbor, MI 48109-1107, USA
[11] European Southern Observatory, K. Schwarzschild-Strasse 2, D-85748 Garching bei Munchen, Germany
[12] Department of Astronomy, Harvard University, 60 Garden Street, Cambridge, MA 02138, USA
[13] ECAP-Erlangen Centre for Astroparticle Physics, Sternwartstrasse 7, D-96049 Bamberg, Germany
[14] NASA Goddard Space Flight Center, Greenbelt, MD 20771, USA

Received 2016 March 18; revised 2016 April 29; accepted 2016 May 11; published 2016 July 25

ABSTRACT

We present a multi-epoch hard X-ray analysis of Cygnus X-1 in its soft state based on four observations with the *Nuclear Spectroscopic Telescope Array* (*NuSTAR*). Despite the basic similarity of the observed spectra, there is clear spectral variability between epochs. To investigate this variability, we construct a model incorporating both the standard disk-corona continuum and relativistic reflection from the accretion disk, based on prior work on Cygnus X-1, and apply this model to each epoch independently. We find excellent consistency for the black hole spin and the iron abundance of the accretion disk, which are expected to remain constant on observational timescales. In particular, we confirm that Cygnus X-1 hosts a rapidly rotating black hole, $0.93 \lesssim a^{*} \lesssim 0.96$, in broad agreement with the majority of prior studies of the relativistic disk reflection and constraints on the spin obtained through studies of the thermal accretion disk continuum. Our work also confirms the apparent misalignment between the inner disk and the orbital plane of the binary system reported previously, finding the magnitude of this warp to be $\sim 10^{\circ}$–15°. This level of misalignment does not significantly change (and may even improve) the agreement between our reflection results and the thermal continuum results regarding the black hole spin. The spectral variability observed by *NuSTAR* is dominated by the primary continuum, implying variability in the temperature of the scattering electron plasma. Finally, we consistently observe absorption from ionized iron at ~6.7 keV, which varies in strength as a function of orbital phase in a manner consistent with the absorbing material being an ionized phase of the focused stellar wind from the supergiant companion star.

Key words: black hole physics – X-rays: binaries – X-rays: individual (Cygnus X-1)

1. INTRODUCTION

Cygnus X-1, the first X-ray binary confirmed to host a black hole accretor (Murdin & Webster 1971; Tananbaum et al. 1972; Gies & Bolton 1986a), is one of the best studied Galactic black hole binaries (BHBs). This system consists of a $\sim 14.8\,M_{\odot}$ black hole (Orosz et al. 2011) accreting from the stellar wind of a type O9.7Iab supergiant companion (HDE 226868; Walborn 1973), and is one of the closest black hole systems known ($D = 1.86$ kpc; Reid et al. 2011).

Besides its proximity, which makes it one of the brightest X-ray sources in the sky, Cygnus X-1 is an important system because it exhibits one of the best established examples of relativistic reflection from the inner regions of its accretion disk (e.g., Fabian et al. 1989; Miller et al. 2002; Reis et al. 2010; Duro et al. 2011; Fabian et al. 2012). This reflection is produced when the accretion disk is irradiated by hard X-rays, and is dominated by iron K α emission (~6–7 keV, depending on ionization state) and a characteristic high-energy continuum peaking at ~20–30 keV (the Compton hump; e.g., George & Fabian 1991). While the line emission is intrinsically narrow, relativistic effects associated with the motion of the accreting material and the extreme gravitational potential close to the black hole distort this emission into a broad "diskline" profile (Fabian et al. 1989; Laor 1991; Brenneman & Reynolds 2006; Dauser et al. 2010). Relativistically broadened iron lines are observed in both Galactic BHBs and active galactic nuclei (AGNs), e.g., Walton et al. (2012). Study of these distortions can provide geometric constraints on both the inner accretion disk, and in turn the spin of the black hole (e.g., Walton et al. 2013b; Reynolds 2014), and the source of the illuminating hard X-rays (e.g., Wilkins & Fabian 2012). The hard X-ray source is believed to be due to a plasma of hot electrons, referred to as the "corona," which up-scatters the blackbody emission from the accretion disk into a power-law–like high-energy continuum.

The *Nuclear Spectroscopic Telescope Array* (*NuSTAR*; Harrison et al. 2013) covers the 3–79 keV band with unprecedented sensitivity above 10 keV. This makes *NuSTAR* ideally suited to study relativistic disk reflection, because its broad bandpass enables simultaneous measurements of both the

Table 1
The Soft State *NuSTAR* Observations of Cygnus X-1 Considered in this Work

Epoch	Orbital Phase[a]	OBSID	Start Date	Exposure[b] (ks)
1	0.26–0.37	00001011001	2012 Jul 02	14.4 (4.1)
		00001011002		5.2 (1.5)
2	0.97–0.09	10002003001	2012 Jul 06	12.5 (3.5)
3	0.85–0.99	30001011002	2012 Oct 31	11.0 (0.9)
		30001011003		5.7 (0.6)
		10014001001		4.6 (0.4)
4	0.46–0.59	30001011009	2014 Oct 04	22.6 (2.2)

Notes.
[a] Based on the ephemeris of Gies et al. (2008).
[b] The mode 6 contribution to the total exposure is given in parentheses.

iron emission and the Compton hump. Furthermore, its triggered read-out means *NuSTAR* is also well suited to deal with the high count-rates from Galactic BHBs, providing a clean, high signal-to-noise measurement of the spectra of these sources. Since launch, *NuSTAR* has performed a series of observations to study relativistic reflection in this population (e.g., Miller et al. 2013; King et al. 2014; Fürst et al. 2015; Tao et al. 2015; Parker et al. 2016). In addition, owing to its bandpass, *NuSTAR* is also well positioned to provide constraints on the high-energy emission from the corona (e.g., Miller et al. 2013; Natalucci et al. 2014; Fabian et al. 2015).

As part of its program to observe reflection in Galactic BHBs, *NuSTAR* has performed a series of observations of Cygnus X-1 (Tomsick et al. 2014; Parker et al. 2015), covering both the "soft" (disk dominated) and "hard" (corona dominated) accretion states (see Remillard & McClintock 2006 for a review of Galactic BHB accretion states). To date, these studies have found that Cygnus X-1 hosts a rapidly rotating black hole. This is in good agreement with previous reflection-based results (e.g., Duro et al. 2011, 2016; Fabian et al. 2012; Miller et al. 2012), as well as results from a detailed study of the blackbody disk emission (e.g., Gou et al. 2011, 2014). The *NuSTAR* observations also found evidence that the innermost accretion disk might be misaligned with the orbital plane of the binary system (Tomsick et al. 2014; Parker et al. 2015).

Soft state observations are particularly important for testing models of relativistic disk reflection. It is widely accepted that in this state the accretion rate is high enough for the disk to extend to the innermost stable circular orbit (ISCO), which is necessary to measure black hole spin. Here, we present multi-epoch broadband X-ray observations of Cygnus X-1 with *NuSTAR*, with the purpose of examining the spectral variability and the relativistic disk reflection exhibited during its soft, disk-dominated accretion state. The paper is structured as follows: in Section 2 we describe the *NuSTAR* observations and outline our data reduction procedure, in Sections 3 and 4 we present our spectral analysis of these data and discuss the results obtained, and finally in Section 5 we summarize our conclusions.

2. OBSERVATIONS AND DATA REDUCTION

NuSTAR performed soft state observations of Cygnus X-1 at four epochs prior to 2015, either as a science target (OBSIDs beginning with 3) or as an early mission calibration target (OBSIDs beginning with 0 or 1); see Table 1 for details. Figure 1 shows how these observations relate to the long-term behavior seen from Cygnus X-1 by both *MAXI* (Matsuoka et al. 2009) and *Swift* BAT (Barthelmy et al. 2005). Although multiple OBSIDs are listed for some epochs, these are actually continuous observations. The science exposures from epoch 3 (OBSIDs 30001011002 and 30001011003) have already been presented in Tomsick et al. (2014). However, immediately after those observations *NuSTAR* performed a further calibration exposure. In this work, we utilize the data from all three of these exposures. The rest of the observations included in this work are published here for the first time.

We reduced the *NuSTAR* observations using the standard pipeline, which is part of the *NuSTAR* Data Analysis Software v1.4.1 (NUSTARDAS; part of the HEASOFT distribution), adopting instrumental responses from *NuSTAR* CALDB version 20150316 throughout. The unfiltered event files were cleaned with the standard depth correction, which significantly reduces the instrumental background at high energies. Periods of Earth-occultation and passages through the South Atlantic Anomaly were excluded. Source products were obtained from large circular regions (radius $\sim 150''$) for each of the two focal plane modules (FPMs A and B). Owing to its brightness, no regions of the detector on which Cygnus X-1 was located were free of source counts, so the background was estimated from a blank region on the opposite detector (each FPM carries four detectors in a square formation; see Harrison et al. 2013), sufficiently far away from the position of Cygnus X-1 to avoid any contribution from the source. Because of the variations in the background between the detectors for each FPM, estimating the background from a different detector to the source may formally introduce some systematic uncertainty. However, these differences are typically only at the $\sim$10% level (in the background rate) at the highest energies of the *NuSTAR* bandpass (where the internal detector background dominates; Wik et al. 2014). All soft state spectra obtained from Cygnus X-1 are a factor of $\sim$3 or more above the background even at these energies, and this increases very quickly toward lower energies with the source typically a factor of $\sim$1000 above the background at the low end of the *NuSTAR* bandpass, so systematic effects due to background should have a negligible influence on our results.

In addition to the standard "science" data (hereafter mode 1), we also reduce the available "spacecraft science" data (referred to as mode 6) to utilize the maximum possible exposure from each observation. In brief, this is the data recorded during the observation periods for which the X-ray source is still visible, but the star tracker on the optics bench cannot return a good aspect solution, so the star trackers on board the spacecraft bus are used instead (see Appendix). This provides an additional 10%–40% live time, depending on the observation (see Table 1). For epochs with multiple OBSIDs, the data from each observation were reduced separately, and the individual spectra from each FPM were then combined into a single average spectrum from that epoch using ADDASCASPEC; we do not combine the data from FPMA and FPMB, as recommended (Madsen et al. 2015). The resulting spectra from each FPM and each epoch were grouped to have a minimum of 50 counts per bin to facilitate the use of χ^2 statistics in our analysis.

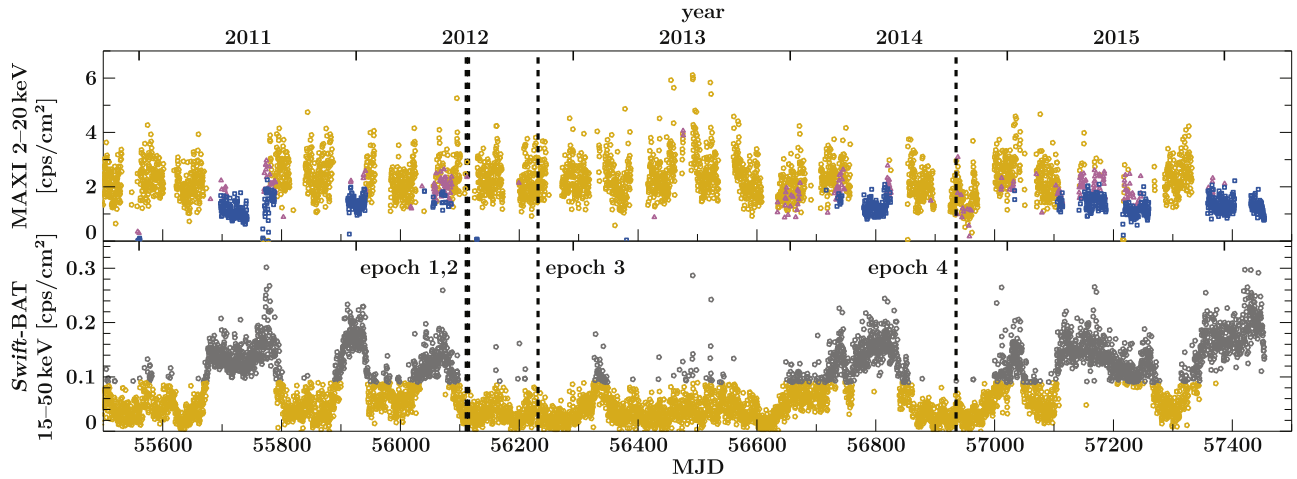

Figure 1. Long-term X-ray light curves (6 hr bins) for Cygnus X-1 observed with *MAXI* (top panel) and *Swift* BAT (bottom panel) since ∼2011, with the *NuSTAR* observations considered in this work shown (dashed lnes). For the *MAXI* light curve, soft states are shown in yellow, intermediate states in magenta, and hard states in blue, following the definitions of Grinberg et al. (2013). For the *Swift* BAT light curve, soft states are shown in yellow, and gray indicates either hard or intermediate states (which cannot easily be distinguished with the higher energy bandpass of the BAT detectors).

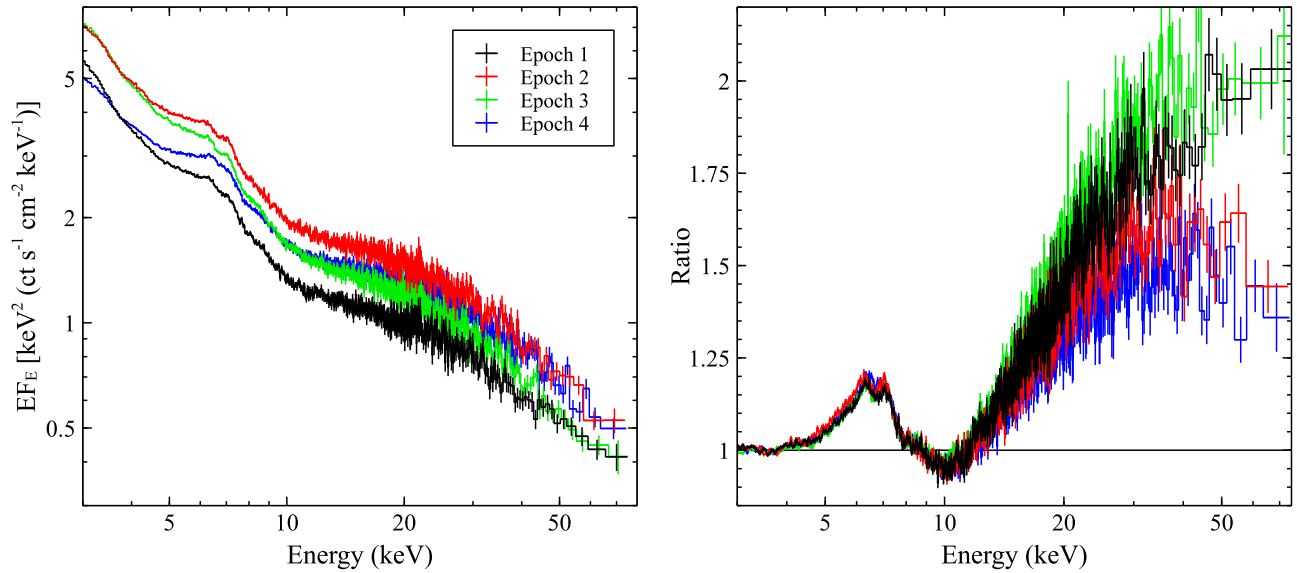

Figure 2. Left panel: The X-ray spectra from the four *NuSTAR* observations of Cygnus X-1 in its soft state. The spectra have been unfolded through a model that is constant with energy. Right panel: Data/model ratios for these data after being fit with a simple model consisting of an accretion disk and a high-energy power-law tail, fit to the 3–4, 8–10, and 50–79 keV bands. In each case, the residuals imply the presence of a strong reflection component from the accretion disk (see Tomsick et al. 2014). Notably, a relativistically broadened iron line is seen in all four *NuSTAR* soft state observations. While the residuals are broadly similar for all epochs, there are visible differences at the highest energies probed by *NuSTAR*. For both panels, the data have been further rebinned for visual purposes, and only the FPMA data are shown for clarity.

3. SPECTRAL ANALYSIS

To investigate the spectral variability exhibited by Cygnus X-1 in its soft state, we perform a detailed comparison of the *NuSTAR* data from each of the four epochs considered here. Throughout this work, our spectral analysis is performed with XSPEC v12.6. 0f Arnaud (1996). All our models include a neutral Galactic absorption component, modeled with TBABS (Wilms et al. 2000). However, because *NuSTAR* is not particularly sensitive to the typical column ($N_{\rm H} \sim 6 \times 10^{21}$ cm^{-2}; e.g., Tomsick et al. 2014) owing to its bandpass (3–79 keV), we fix the neutral absorption to 6×10^{21} cm^{-2} for simplicity.[15] We adopt the abundances in Wilms et al. (2000) as our "solar" abundance set, as appropriate for absorption by the Galactic interstellar medium, and adopt the recommended cross-sections of Verner et al. (1996). Parameter uncertainties are quoted at 90% confidence for one parameter of interest throughout this work, and we account for residual cross-calibration flux uncertainties between the FPMA and FPMB detectors by allowing multiplicative constants to float between them, fixing FPMA to unity. The FPMB constants are always found to be within 5% of unity, as expected (Madsen et al. 2015).

The *NuSTAR* spectra obtained from each of the four epochs are shown in the left panel of Figure 2. Although all four are broadly quite similar, there are clear differences observed from epoch to epoch. This is further demonstrated in the right panel of the same Figure, which shows data/model ratios to a

[15] Note that as outlined by Grinberg et al. (2015), this is only appropriate for the soft state, because the stellar wind is highly ionized and has little effect on the neutral absorption (see also Nowak et al. 2011).

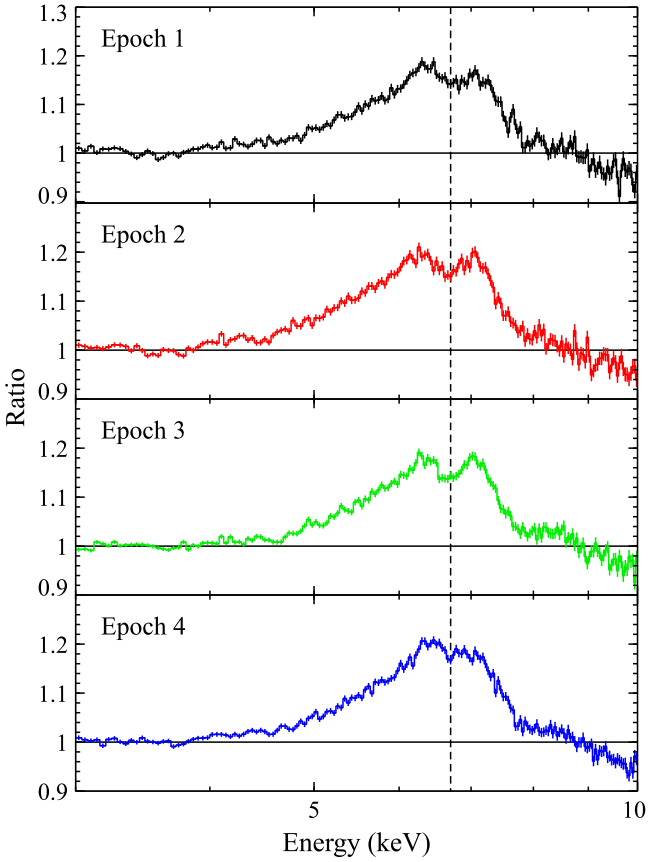

Figure 3. The same data/model residuals shown in Figure 2 (right panel), zoomed in on the iron K α bandpass to highlight the iron emission. The line profiles from each *NuSTAR* observation are all very similar. In addition to the relativistically broadened iron emission, absorption of variable strength from ionized iron can be seen at ∼6.7 keV (the vertical dashed line shows E = 6.7 keV). The data have been further rebinned for visual clarity.

continuum model consisting of a multi-temperature blackbody accretion disk (DISKBB; Mitsuda et al. 1984) with a high-energy power-law tail, fit to the spectrum over the 3–4, 8–10, and 50–79 keV energy ranges to minimize the influence on the model fit of the disk reflection spectrum known to be present (e.g., Duro et al. 2011; Fabian et al. 2012; Tomsick et al. 2014). There are clear differences between epochs in the residuals from such a model at the highest energies probed by *NuSTAR*. In contrast, the profile of the iron emission inferred with this continuum appears to be rather stable; we show a zoom in on the iron residuals in Figure 3. The broad iron emission is strong in the soft state; adding a RELLINE component (Dauser et al. 2010) to the simple continuum model described above and fitting the 3–10 keV band, we find equivelent widths of EW ∼ 300–330 eV for all four epochs. An absorption feature associated with ionized iron is also visually apparent in the residuals at ∼6.7 keV for some epochs, but its strength appears to be variable.

3.1. Model Setup

We construct a spectral model for Cygnus X-1 building on the soft state analysis presented in Tomsick et al. (2014). Similar to the majority of models considered in that work, our model consists of an accretion disk component (DISKBB), a high-energy power-law tail with an exponential high-energy cutoff representing the coronal emission (CUTOFFPL), a disk reflection component to account for the iron emission and the reflected continuum observed at higher energies (using the XILLVER reflection code and the RELCONV model to account for the relativistic effects close to the black hole; García & Kallman 2010 and Dauser et al. 2010, respectively), and absorption from an ionized plasma to account for the 6.7 keV iron absorption feature (XSTAR; Kallman & Bautista 2001).

Our choice of models is largely driven by pragmatic considerations. For the reflected emission, we use the XILLVER reflection model because it incorporates the effects of viewing angle (i.e., the disk inclination, i) on the observed reflection spectrum. We use the combination of XILLVER and RELCONV to remain consistent with the approach of Tomsick et al. (2014). The XILLVER family of reflection models is calculated assuming a slab temperature of 10 eV. This is appropriate for accretion disks around active galaxies, but is much cooler than the disk temperatures observed from X-ray binaries, and thus the Compton broadening of the iron emission emerging from the accretion disk will be underpredicted (e.g., Ross & Fabian 2007). Therefore, before applying the RELCONV model, we additionally smooth the XILLVER model with a Gaussian to approximate this additional broadening. This is similar to Model 9 in Tomsick et al. (2014), but here rather than allow this broadening to be an additional free parameter, we explicitly link it to the disk temperature (i.e., we assume that the free electrons within the disk also have this temperature). The amount of broadening (σ) is then given by $\sigma/E = \sqrt{2kT_{\rm e}/m_{\rm e}c^2}$, where E is the line energy, k is Boltzmann's constant, $T_{\rm e}$ is the electron temperature, $m_{\rm e}$ is the electron rest mass, and c is the speed of light (Pozdnyakov et al. 1983). Given the ionization of the disk inferred in Tomsick et al. (2014), we also assume hydrogen-like iron is the dominant species and adopt a typical line energy of ∼7 keV.

This choice of reflection model and our treatment of the additional Compton broadening also drive our choice of models for the other continuum components. For the disk emission, we use DISKBB because it explicitly has the temperature as a free parameter ($kT_{\rm in}$), such that we can easily determine the amount of Compton broadening to include. For the coronal emission, we use a CUTOFFPL model even though this is only an approximation of the thermal Comptonization spectrum that may be expected from the corona,[16] because this is the input spectrum assumed in the XILLVER model, and we can therefore easily link the parameters of the high-energy continuum that irradiates the disk (the photon index Γ and cutoff energy $E_{\rm cut}$) to those of the continuum component included in the model. There has recently been some indication from *NuSTAR* observations of Galactic BHBs that the disk might be irradiated by a different hard X-ray continuum than that emitted along our line of sight (Fürst et al. 2015; Parker et al. 2015), likely owing to a complex combination of radial variations in the spectrum of the coronal emission, potential outflow velocity gradients, and gravitational lightbending (Fabian et al. 2014). However, these

[16] There may also be a weak power-law contribution from Comptonization by non-thermal electrons visible at extremely high (∼MeV) energies (e.g., McConnell et al. 2002; Laurent et al. 2011), but this cannot be constrained by our *NuSTAR* observations and so is not included in the model. When we refer to the high-energy tail or the power-law component in this work, we are referring to our approximation of the thermal Comptonization.

have come from hard state observations in which the corona might be more significantly extended and/or outflowing (perhaps being associated with the base of the jets launched in this state; Markoff et al. 2005; Miller et al. 2012), where such variations might naturally be expected. In contrast, the corona is generally expected to be more compact in the soft state (e.g., Reis et al. 2013), and radio jets are absent in this state (e.g., Fender et al. 2004), thus the corona may well be more static than in the hard state. We therefore assume that these effects would be much less significant in the soft state and the continuum irradiating the disk is the same as that observed, noting that this has previously worked well for the soft state (Tomsick et al. 2014). Following García et al. (2015), we consider cutoff energies $E_{\rm cut} \leqslant 1$ MeV.

The other key free parameters for the reflection model are the black hole spin (a^*), the iron abundance ($A_{\rm Fe}$) of the disk, its inclination (i) and its ionization parameter ($\xi = L/nR^2$, where L is the ionizing luminosity, n the density, and R the distance to the ionizing source), and the radial emissivity profile of the reflected emission. We assume that the disk extends to the innermost stable circular orbit (ISCO), as is also generally expected for the soft state, and set the outer radius to the maximum value allowed by the RELCONV model ($400\,R_{\rm G}$). The emissivity profile is assumed to be a broken power law (i.e., $\epsilon(r) \propto r^{-q}$, where the emissivity indices $q_{\rm in,out}$ differ on either side of some break radius $R_{\rm br}$). Following Fabian et al. (2012), we assume $q_{\rm out}$ to be 3 (as expected in the simple Newtonian case; Reynolds & Begelman 1997), and leave $q_{\rm in}$ and $R_{\rm br}$ to be free parameters.

We also allow for the presence of a narrow ($\sigma = 10$ eV) Gaussian emission line from neutral iron (6.4 keV) in the model to account for X-ray illumination of the wind launched from the massive stellar companion of Cygnus X-1. Narrow iron emission lines are typically observed from high-mass X-ray binaries (e.g., Torrejón et al. 2010), and the iron emission from Cygnus X-1 has previously been observed to be a composite of a broad and narrow component (e.g., Miller et al. 2002; Reis et al. 2010). As such, in XSPEC notation, the final form of our model is TBABS$\times$ XSTAR $\times$ (DISKBB + CUTOFFPL + GAUSSIAN + RELCONV $\otimes$ XILLVER.

Finally, for consistency, the XSTAR model used for the ionized iron absorption is the same as that used in Tomsick et al. (2014). This is computed with XSTAR version 2.2.1bg, with the ionization parameter and the column density of the absorbing medium set as free parameters. Elemental abundances are assumed to be solar, and the model is computed with a density of 10^{12} cm^{-3} and a turbulent velocity of 300 km s^{-1}(Miller et al. 2005; Hanke et al. 2009). The input ionizing spectrum is based on a simple model for the soft state of Cygnus X-1 from Tomsick et al. (2014). In addition to the ionization and the column density, we also allow the line-of-sight velocity of the absorbing medium (v) to be another free parameter in our analysis.

We apply this same model to the spectra from each of the four epochs independently to investigate the origin of the observed spectral variability. During the course of our analysis, we found that the ionization of the absorber was difficult to constrain, with statistically similar fits ($\Delta\chi^2 \lesssim 10$) obtained for each observation for solutions with $\log \xi_{\rm abs} \sim 3.8$ and $\log \xi_{\rm abs} \sim 5$ (where ξ is in units of erg cm s^{-1}); three of the four epochs marginally preferred the lower ionization solution, while the remaining epoch (epoch 1) marginally preferred the higher-ionization solution. We attribute the multiple solutions found here to parameter degeneracies in the absorption model that can occur when fitting a single, ionized iron absorption line (e.g., King et al. 2014). However, given the level of variability apparent in Figure 2, the ionization is unlikely to differ by more than an order of magnitude between epochs. Furthermore, we found that the higher-ionization solution required the absorption to be significantly redshifted, because it was fitting the feature at ~6.7 keV with a blend of Fe XXV (6.67 keV) and Fe XXVI (6.97 keV), which we deemed to be unphysical. In our final analysis we therefore limit $\log \xi_{\rm abs} < 4$ and only allow the absorption to be blueshifted (i.e., outflowing) to exclude these higher-ionization solutions.

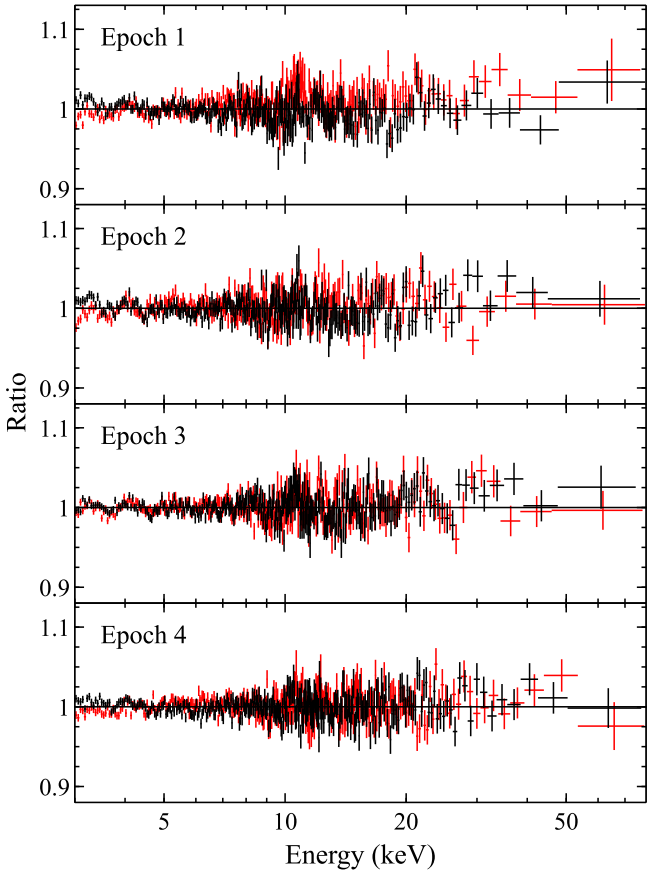

Figure 4. Data/model residuals for our final relativistic disk reflection model (see Section 3.1). For each of the four epochs, FPMA data are shown in black and FPMB in red. Our model fits each of the soft state *NuSTAR* observations well. As before, the data have been further rebinned for visual clarity.

3.2. Results

Our final model provides a good fit to all four soft state epochs observed by *NuSTAR* to date. Data/model residuals are shown in Figure 4, and the best-fit parameters obtained are given in Table 2. No strong residuals remain across the entire *NuSTAR* bandpass.

Some noteworthy results are immediately apparent from a comparison of the best-fit parameters obtained. First, the key disk reflection parameters that should remain constant with time are consistent across all four epochs (see Figure 5). The consistency of the black hole spin confirms that the inner disk radius remains constant during the soft state, as expected if the disk extends all the way into the ISCO. It also further reinforces

Table 2
Results Obtained for the Free Parameters in the Disk Reflection Model Constructed in this Work

Model Component	Parameter		Epoch 1	Epoch 2	Epoch 3	Epoch 4
DISKBB	$kT_{\rm in}$	[keV]	$0.405^{+0.010}_{-0.005}$	0.44 ± 0.01	0.47 ± 0.01	0.45 ± 0.01
	Norm	[10^4]	15^{+2}_{-3}	9^{+2}_{-3}	$6.2^{+0.6}_{-1.4}$	$4.3^{+1.3}_{-0.2}$
CUTOFFPL	Γ		2.69 ± 0.01	2.58 ± 0.02	$2.74^{+0.03}_{-0.04}$	$2.56^{+0.02}_{-0.01}$
	$E_{\rm cut}$	[keV]	>600	160^{+30}_{-30}	280^{+110}_{-70}	210^{+20}_{-40}
	Norm (at 1 keV)	[cts keV^{-1} cm^{-2} s^{-1}]	$5.2^{+0.3}_{-0.4}$	$6.3^{+0.2}_{-0.3}$	8.0 ± 0.2	5.2 ± 0.1
RELCONV	a^*		$0.948^{+0.006}_{-0.010}$	$0.937^{+0.008}_{-0.007}$	$0.939^{+0.008}_{-0.007}$	0.946 ± 0.008
	i	[°]	$40.7^{+0.4}_{-0.8}$	$38.2^{+0.9}_{-0.6}$	$39.4^{+0.5}_{-0.7}$	$40.8^{+0.5}_{-0.4}$
	$q_{\rm in}$		>9.4	>7.5	>6.1	>8.6
	$R_{\rm br}$	[$R_{\rm G}$]	$2.89^{+0.07}_{-0.04}$	$2.91^{+0.42}_{-0.07}$	$3.3^{+0.2}_{-0.4}$	$2.63^{+0.09}_{-0.06}$
XILLVER	$\log \xi_{\rm refl}$	log[erg cm s^{-1}]	$4.05^{+0.06}_{-0.02}$	$4.02^{+0.03}_{-0.02}$	$4.02^{+0.04}_{-0.02}$	$3.82^{+0.03}_{-0.05}$
	$A_{\rm Fe}$	[solar]	$4.2^{+0.3}_{-0.4}$	$4.2^{+0.6}_{-0.4}$	$4.3^{+0.4}_{-0.3}$	4.0 ± 0.3
	Norm	[10^{-6}]	$3.5^{+0.4}_{-0.8}$	$4.0^{+0.4}_{-0.6}$	$5.7^{+0.5}_{-0.7}$	$4.0^{+1.0}_{-0.3}$
XSTAR	$N_{\rm H}$	[10^{21} cm^{-2}]	$5.7^{+0.8}_{-0.6}$	9^{+2}_{-1}	$9.3^{+1.5}_{-0.9}$	$4.5^{+0.7}_{-2.3}$
	$\log \xi_{\rm abs}$	log[erg cm s^{-1}]	>3.9	$3.6^{+0.2}_{-0.1}$	3.7 ± 0.2	$3.6^{+0.2}_{-0.1}$
	$v_{\rm out}$	[km s^{-1}]	700^{+1500}_{-600}	<600	<800	3500^{+300}_{-2000}
GAUSSIAN	Line Flux[a]	[10^{-12} erg cm^{-2} s^{-1}]	$5.6^{+1.5}_{-1.4}$	$3.2^{+3.4}_{-2.8}$	$3.4^{+2.7}_{-1.5}$	$8.5^{+1.9}_{-1.2}$
	Equivalent Width	eV	<40	<100	<14	10^{+5}_{-4}
χ^2/dof			2049/1758	1978/1718	2089/1783	2080/1958

Note.
[a] Calculated under the assumption that the narrow core of the line is present in all observations.

the conclusion that Cygnus X-1 hosts a rapidly rotating black hole, as found by previous disk reflection spectroscopy (e.g., Fabian et al. 2012), and from study of the thermal continuum (e.g., Gou et al. 2011, 2014). In our model setup, the disk temperatures obtained imply an expected Compton broadening of $\sigma \sim 0.3$ keV for all epochs, which is similar to that obtained by Tomsick et al. (2014), who allowed this to be an additional free parameter (see their Model 9). This is clearly insufficient to explain the full breadth of the observed iron emission, and does not change the requirement for additional relativistic broadening.

Excellent consistency is also obtained for the iron abundance, which is found to be super-solar. The abundance obtained here is higher than presented in Tomsick et al. (2014), although we note that Tomsick et al. (2014) use of the REFLIONX model (Ross & Fabian 2005), whereas we use the XILLVER reflection model. The abundance obtained here is quite similar to that obtained by Parker et al. (2015), who also use the XILLVER model in their analysis of a recent broadband observation of Cygnus X-1 by *Suzaku* and *NuSTAR* in the hard state performed ~5 months prior to our epoch 4.

The ~40° disk inclination inferred with our model is also consistent across all four epochs. As discussed in Tomsick et al. (2014), this is significantly larger than the inclination at which we view the orbital plane of the system ($i_{\rm orb} = 27.^{\circ}1 \pm 0.^{\circ}8$; Orosz et al. 2011). We find that this apparent misalignment is not confined to the single soft state epoch considered in Tomsick et al. (2014), and does not show any evidence of varying on the timescales covered by our observations. Furthermore, the inclination obtained here is similar to that found by Parker et al. (2015), so it does not appear to be confined to the soft state either. Prior studies of relativistic reflection from accreting black holes have found that the black hole spin and the inclination inferred for the accretion

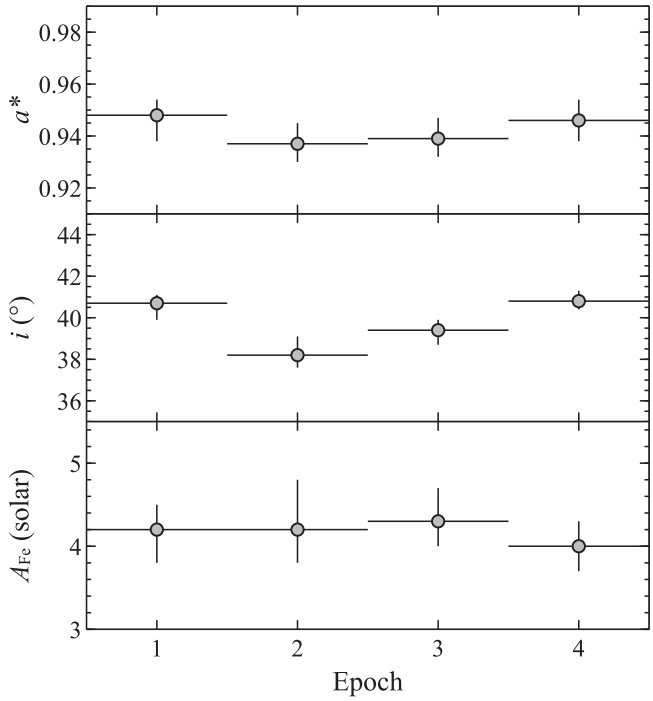

Figure 5. The results obtained for the black hole spin (top panel), the disk inclination (middle panel), and the iron abundance (bottom panel) from our independent analysis of each epoch. These quantities should not change on observable timescales, and indeed good consistency is observed between the different epochs.

disk often show some degree of degeneracy, so in Figure 6 we compute two-dimensional confidence contours for these parameters. While the degree of degeneracy seen here varies somewhat between epochs, it is very mild and not sufficient to reconcile the measured inner disk inclination with the orbital

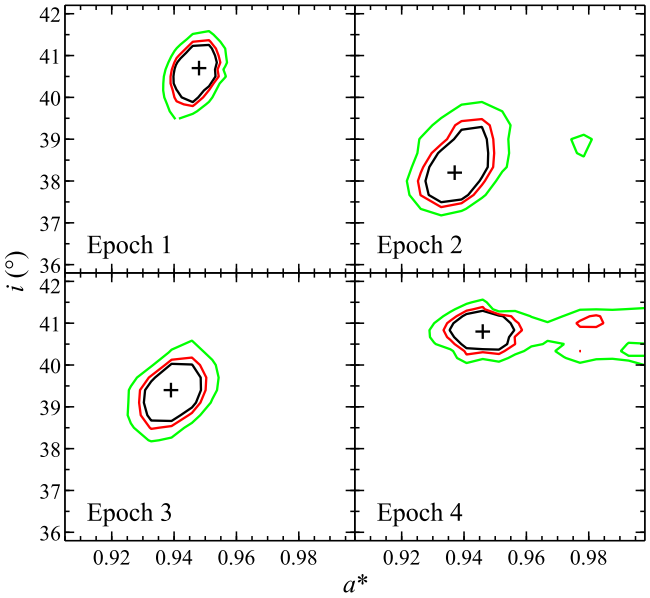

Figure 6. Two-dimensional $\Delta\chi^2$ confidence contours for the black hole spin (a^*) and the accretion disk inclination (i) for each epoch. The 90, 95, and 99% confidence intervals for two parameters of interest are shown in black, red, and green, respectively.

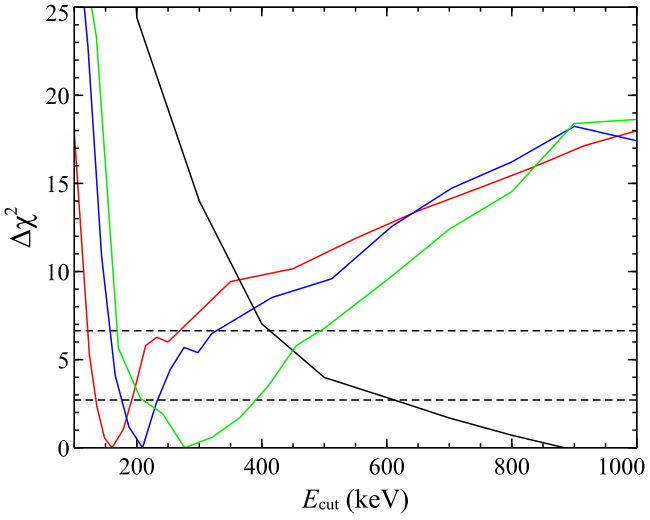

Figure 7. The $\Delta\chi^2$ confidence contours for the high-energy cutoff ($E_{\rm cut}$) for each of the four soft state *NuSTAR* observations. The contours for epochs 1, 2, 3, and 4 are shown in black, red, green, and blue, respectively. The horizontal dashed lines represent the 90% and 99% confidence levels for a single parameter of interest.

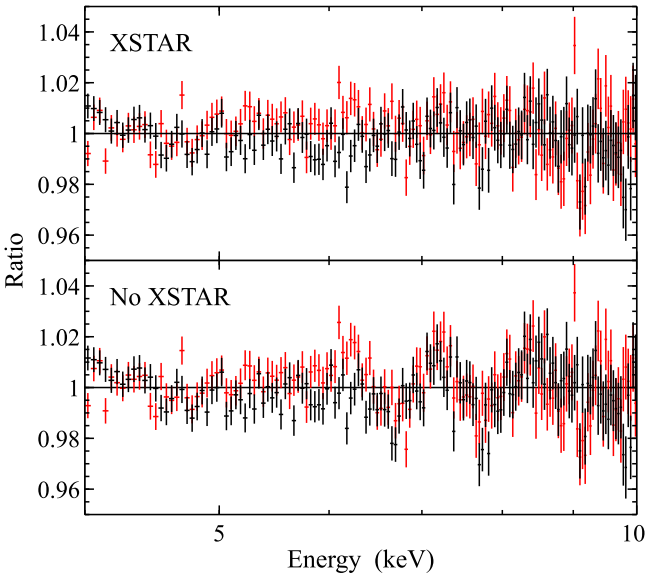

Figure 8. Data/model residuals for epoch 4, zoomed in on the iron K α band. The top panel shows our best-fit reflection model, including ionized iron absorption (modeled with XSTAR), and the bottom panel shows the best fit for the same model but with the ionized absorption removed. Although the absorption is much weaker during this epoch, it is still required to fit the data. As before, the data have been further rebinned for plotting purposes; colors are as in Figure 4.

plane measurement. Indeed, an inner disk inclination of ~27° is strongly disfavored by our current model; for illustration, we fit epoch 1 with the inclination fixed to 27°.1, resulting in the fit degrading by $\Delta\chi^2 = 450$ and noticeable residuals around the blue wing of the iron line. However, it is worth noting that even with this fit, the spin inferred for Cygnus X-1 is high ($a^* > 0.91$).

In contrast to the stability of the disk reflection parameters, we find evidence for variability in the high-energy continuum parameters. Most notably, the cutoff energy—which is indicative of the electron temperature assuming that the high-energy continuum is dominated by thermal Comptonization—is found to vary between epochs by at least a factor of ~3–4 (ranging from ~150 up to >600 keV; see Figure 7), resulting in the differences at the highest energies probed by *NuSTAR* seen in Figure 2. The range of values obtained here is broadly similar to recent results obtained for the soft state with the high-energy detectors on board *INTEGRAL*, although these were averaged over several epochs (Jourdain et al. 2014; Rodriguez et al. 2015).

We also confirm the visual indication from Figure 3 that the strength of the absorption at ~6.7 keV is variable, with the column density obtained for the ionized absorbing medium varying from epoch to epoch. We also note that despite not being visually apparent, this absorption is strongly required in the fourth epoch. Excluding the XSTAR component from the model for this epoch results in a significantly worse fit ($\Delta\chi^2 = 109$ for three fewer free parameters), and, as shown in Figure 8, leaves clear absorption residuals. It is only after accounting for the relativistic disk reflection that the imprint of this absorption becomes obvious.

Finally, with regard to the narrow core of the iron emission, we find that this is strongly required for epoch 4 ($\Delta\chi^2 = 78$ for one additional free parameter), and also gives a moderate improvement for epoch 1 ($\Delta\chi^2 = 14$). In contrast, for epochs 2 and 3 including the narrow core does not really provide a meaningful improvement to the fit ($\Delta\chi^2 = 4$ and 7, respectively). Nevertheless, under the assumption that the narrow core is present at each epoch, we still calculate the line flux, which we find to show some level of variability between epochs (unsurprisingly being strongest during epoch 4). We also compute the equivalent width using the EQWIDTH command in XSPEC, but only obtain upper limits for epochs 1, 2, and 3, owing to a combination of the weak statistical improvement this feature provides and the complexity of the underlying continuum model.

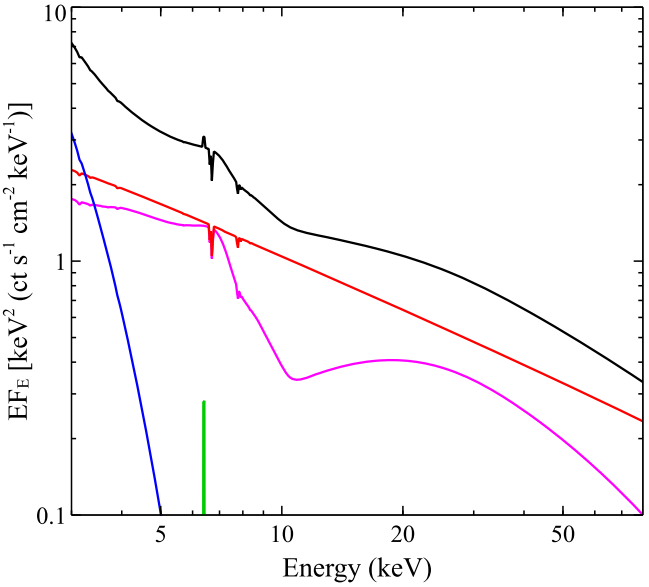

Figure 9. The best-fit disk reflection model obtained for our epoch 1. The total model is shown in black, and the relative contributions across the *NuSTAR* bandpass from the accretion disk (blue), the high-energy power-law tail (red), the disk reflection (magenta), and the narrow core of the iron emission (green) are also shown.

4. DISCUSSION

We have presented a multi-epoch, hard X-ray (3–79 keV) analysis of the canonical black hole high-mass X-ray binary Cygnus X-1 in its soft state with *NuSTAR*. *NuSTAR* has observed Cygnus X-1 in this state on four separate epochs prior to 2015. One of the great advantages *NuSTAR* has when studying sources as bright as Cygnus X-1 is that it does not suffer from pile-up, owing to its triggered read-out (Harrison et al. 2013), and thus provides a clean, high signal-to-noise view of the X-ray spectrum. Although we observe some variation between the different epochs (see Figure 2), these observations all show broadly similar spectra with strong disk emission (peaking below the *NuSTAR* bandpass; Tomsick et al. 2014) and a steep high-energy tail ($\Gamma \sim 2.6$; consistent with the soft state criterion outlined by Grinberg et al. 2013). In addition to this continuum emission, each of the four epochs reveals a clear contribution from relativistic reflection from the inner accretion disk (see Figures 2, 3), enabling us to probe the inner accretion geometry, as well as ionized absorption from ionized iron (see Figures 3, 8).

Building on the original work of Tomsick et al. (2014), who present a detailed analysis of the *NuSTAR* data that comprise the majority of our epoch 3, we construct a relativistic disk reflection model and apply this to each of the four epochs independently to investigate the spectral variability observed between them. The best-fit model obtained for epoch 1 is shown in Figure 9, as an example of the relative contributions across the *NuSTAR* bandpass from the different model components.

4.1. Black Hole Spin and the Inner Accretion Disk

Even though there is clear broadband spectral variability, the profile of the iron emission inferred from simple continuum models is found to be very similar for all epochs (Figure 3), implying that the geometry of the accretion disk is stable throughout these observations. Indeed, the quantitative results obtained from our disk reflection modeling show excellent consistency for the key parameters that should not vary on observational timescales (black hole spin, disk inclination, iron abundance; Figure 5). This is similar to the recent multi-epoch analysis of the large *NuSTAR*+*XMM-Newton* campaign on the active galaxy NGC 1365 (Walton et al. 2014), where excellent consistency was also found for the key reflection parameters. It is worth noting that in between these soft state observations Cygnus X-1 underwent at least one transition to a hard state (e.g., between epochs 3 and 4, see Figure 1; Parker et al. 2015), so we are not simply observing one continuous, uninterrupted soft state, but rather a configuration that Cygnus X-1 has returned to on more than one occasion.

Our multi-epoch results present a consistent picture: that Cygnus X-1 hosts a rapidly rotating black hole. Our analysis constrains the spin of Cygnus X-1 to be $0.93 \lesssim a^* \lesssim 0.96$ (based on the 90% statistical uncertainties on the measurements from each epoch). The quantitative results obtained for the spin here (Table 2) are consistent with the majority of the constraints obtained from previous reflection modeling, both from the *NuSTAR* observations analyzed prior to this work (Tomsick et al. 2014; Parker et al. 2015), and from analyses based on observations with *XMM-Newton*, *RXTE*, *Suzaku*, and *INTEGRAL* (e.g., Duro et al. 2011, 2016; Fabian et al. 2012; Miller et al. 2012), despite these works using a range of different reflection models fit over a variety of different bandpasses, and even considering different accretion states. This is also in good agreement with the results obtained through detailed study of the thermal accretion disk emission, which also find a high spin for Cygnus X-1 (Gou et al. 2011, 2014). The consistency between the two techniques leads us to conclude that these measurements are robust, and that Cygnus X-1 hosts a rapidly rotating black hole. While there are still only a few *NuSTAR* spin constraints for Galactic BHBs, owing in large part to the relatively short mission lifetime at the time of writing, we note that there is also excellent consistency between the *NuSTAR* reflection results and the thermal continuum for the only other case we are aware of where both are available, GRS 1915+105 (McClintock et al. 2006; Miller et al. 2013).

The inclination we obtain for the inner disk is ~40° for all epochs, which is broadly consistent with the previous *NuSTAR* results, but significantly larger than the orbital inclination reported by Orosz et al. (2011), $i_{\rm orb} = 27.^{\circ}1 \pm 0.^{\circ}8$, confirming the discrepancy discussed by both Tomsick et al. (2014) and Parker et al. (2015). Currently the best interpretation for this discrepancy relates to a warp in the accretion disk. This would need to be of the order of ~10°–15° based on our results, which may be plausible given the binary population synthesis work of Fragos et al. (2010). Furthermore, the 3D simulations of Nealon et al. (2015) suggest that such warps or misalignments may remain stable, as our results suggest. If this warp is real, in principle this would mean that adopting the orbital inclination when estimating the black hole spin from the thermal accretion disk continuum would not be correct. However, Gou et al. (2011) show the inferred spin as a function of disk inclination (see their Figure 5), and for the inclination found here the result inferred for the spin of Cygnus X-1 changes only marginally. In fact, adopting our inclination improves the formal quantitative agreement between the spin inferred from the thermal continuum, which would change from $a^* \sim 0.998$ to

$a^* \sim 0.96$, and the constraints obtained in this work (see above). However, such differences are likely small in comparison to the systematic errors associated with such measurements (with both techniques), so we consider the agreement to be excellent regardless of whether the inferred warp is real or not.

Finally, we find that the accretion disk has a super-solar iron abundance. While this is driven in part by the strength of the iron emission (see Section 3), it is also influenced by the Compton hump, because the iron absorption helps determine the curvature of the spectrum on its red (low-energy) side. For illustration, we also fit the data from epoch 2 with our model just above 10 keV. The parameters of the DISKBB and XSTAR components were fixed at their best-fit values, as were the inclination and ionization state of the accretion disk, because the data considered are not particularly sensitive to these parameters. The constraint on the iron abundance is considerably weaker, but we still find a lower limit of Fe/solar > 4.4 from the data above 10 keV alone, which is consistent with the results for the full *NuSTAR* bandpass. Interestingly, these data also provide a weak constraint on the spin of $a^* > 0.3$, also consistent with the full band fits.

A high iron abundance is in qualitative agreement with other studies in which it was allowed to vary, even if there is some quantitative tension. Here, the quantitative results are reasonably well split by the reflection model utilized, and when the same model is compared good agreement is seen. Results obtained using the REFLIONX code (Ross & Fabian 2005) generally tend to return Fe/solar ∼2 (e.g., Duro et al. 2011; Fabian et al. 2012; Tomsick et al. 2014)[17], while results obtained with XILLVER-based models (García & Kallman 2010; García et al. 2014) tend to return Fe/solar ∼4 (this work; Parker et al. 2015). Although this may in part be due to the different solar abundance sets adopted by the two models—the REFLIONX models adopt the abundances given in Morrison & McCammon (1983) while the XILLVER models adopt those given in Grevesse & Sauval (1998)—in terms of their Fe/H number ratios, the XILLVER model is only lower by ∼30% (see Table 1 in García et al. 2013), and is insufficient to be the sole cause of this discrepancy. While we conclude that current models do imply that the Cygnus X-1 system has a super-solar iron abundance (under the assumption that the system is chemically homogeneous), the exact abundance still appears to be subject to substantial systematic uncertainties. We note that Hanke et al. (2009) also found evidence for super-solar abundances for elements including iron in the Cygnus X-1 system through high-resolution studies of the absorption in the stellar wind along our line of sight. Dedicated studies undertaking detailed consideration of both the reflection and the absorption simultaneously, utilizing simultaneous broad band and high-resolution observations (with e.g., *Hitomi*; Takahashi et al. 2012) will be required to help further address this issue in the future. We therefore defer a detailed discussion regarding the origin of the super-solar Fe abundance inferred to such future work. However, given that Cygnus X-1 accretes from the stellar wind of its companion, one interesting possibility is that this over-abundance is related to the "first ionization potential effect" seen in some phases of the Solar corona/wind, in which elements with first ionization potential below ∼10 eV (including Fe) show enhanced abundances (see Laming 2015 for a recent review). The exact cause of this effect remains an active area of research. Alternatively, or in combination, metal enrichment from the supernova that produced the black hole powering the Cygnus X-1 system could also result in an enhanced iron abundance.

[17] One noteable exception is the recent work by Duro et al. (2016), who find an abundance of Fe/solar ∼3–4, despite using the REFLIONX model.

4.2. The High-energy Emission

In contrast to the relative stability of the reflection, the primary continuum is variable, driving the observed spectral variability. We formally see some evidence for changes in the temperature of the accretion disk between epochs, but given that the disk emission peaks outside the *NuSTAR* band, we treat this with some caution. The *NuSTAR* band primarily covers the high-energy tail, in which we also see variations in terms of overall slope and, in particular, at the highest energies probed by *NuSTAR* (see Figure 2). While our work only probes the variability of this emission between observing epochs, we note that this also dominates the (intrinsic) short-timescale variability (e.g. Churazov et al. 2001). Although we model this with a simple phenomenological cutoff power-law model for practical reasons, this tail is widely expected to originate through Compton up-scattering of accretion disk photons by a corona of hot electrons (e.g., Haardt & Maraschi 1991). In this case, the energy of the exponential cutoff of the power-law component acts as a proxy for the temperature of the scattering electrons.[18]

We see significant variation in the cutoff energy $E_{\rm cut}$ (see Figure 7), which changes by a factor of $\gtrsim$3–4, driving the variability seen at the top of the *NuSTAR* band. This indicates that the temperature of the scattering electrons varies between epochs. Recently, Fabian et al. (2015) investigated the implications of the high-energy cutoff measurements obtained to date for accreting black holes by *NuSTAR* (for both AGNs and BHBs), finding that the results suggested that the X-ray coronae around these objects are likely in a regime in which pair production/annihilation is important. Our results suggest that this is persistently the case for the soft state of Cygnus X-1, and we speculate that the variability observed in the high-energy cutoff (and thus inferred for the electron temperature) here may indicate the source approaching and receding from the point of catastrophic pair production discussed by Fabian et al. (2015 and references therein).

4.3. Narrow Absorption and Emission

In addition to the high-energy continuum, we also see variability in the strength of the ionized iron absorption at ∼6.7 keV, with some evidence for an orbital dependence. The absorption is stronger at orbital phases when the system is close to inferior conjunction (i.e., the black hole is on the far side of the binary system from our perspective, $\phi_{\rm orb} \sim 0.0$ and $\phi_{\rm orb} \sim 1.0$), and weaker when the system is close to superior conjunection (i.e., $\phi_{\rm orb} \sim 0.5$; see Figure 10, left panel). This is consistent with the absorption arising in an ionized phase of the

[18] We stress however that the conversion between $E_{\rm cut}$ and electron temperature is not necessarily linear, particularly when the inferred cutoff energy is significantly outside the observed bandpass. An exponential cutoff is only a rough approximation of the high-energy cutoff produced by thermal Comptonization, which curves faster with energy once it starts falling away (Zdziarski et al. 2003). While a higher energy cutoff does indicate a hotter electron population, a factor of ∼4 change in $E_{\rm cut}$ does not necessarily imply exactly the same level of variation in the electron temperature. See Fabian et al. (2015) and Fürst et al. (2016) for more discussion.

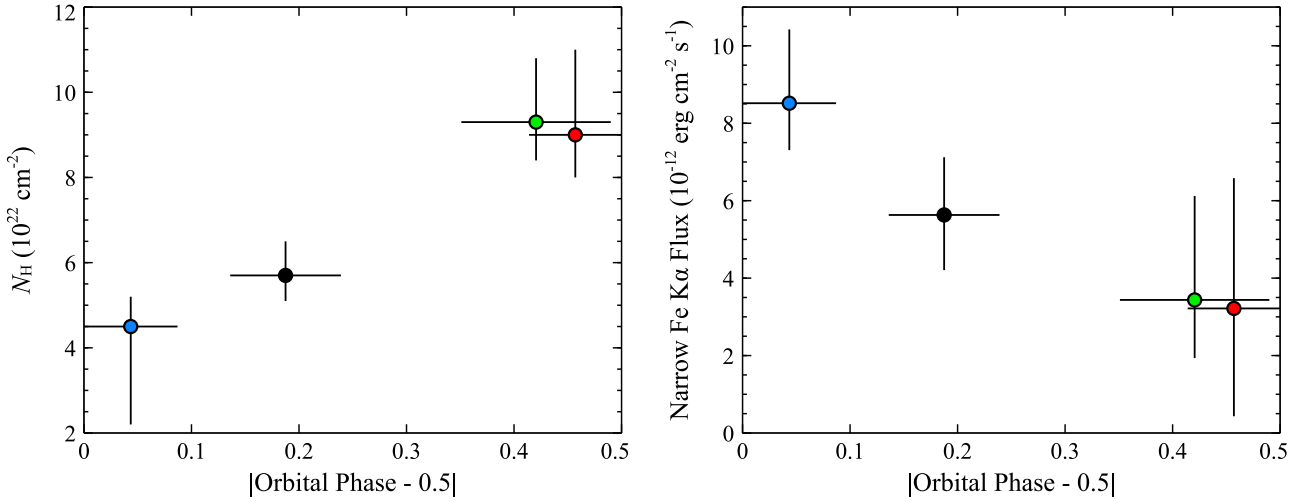

Figure 10. The strength of the ionized iron absorption (left panel) and the flux of the narrow core of the iron emission (right panel; computed assuming this component is present at each epoch) as a function of the orbital phase at which the *NuSTAR* observation was performed. Here we plot the orbital phase in terms of the separation from superior conjunction (i.e., the point at which the companion star is on the far side of the black hole; $\phi_{\rm orb} = 0.5$). As the orbital phase moves away from this point, the strength of the absorption increases. However, the absorption is not completely absent at $\phi_{\rm orb} \sim 0.5$. We also find that the narrow line emission is strongest at this point, although the evidence for this variation is much more marginal. The data points are colored by epoch, following the color scheme in Figures 2 and 3.

stellar wind of the supergiant companion from which Cygnus X-1 accretes, as discussed by, for example, Miller et al. (2005), Hanke et al. (2009), and Nowak et al. (2011). However, despite not being immediately visually obvious, the absorption is not completely absent in our observation that is closest to superior conjunction (epoch 4), suggesting that the stellar wind still pollutes some of the region on the far side of the binary system (with respect to the stellar companion). Grinberg et al. (2015) studied the time evolution of the neutral absorption in detail, primarily during the hard state, and found similar results, including evidence for absorption by the (clumpy) stellar wind even at $\phi_{\rm orb} \sim 0.5$. Interestingly, epoch 4 is also where we see the strongest (although still fairly marginal) evidence for a blueshift in the absorption. It has long been suggested that some portion of the stellar wind from HDE 226868 is focused toward the black hole (e.g., Friend & Castor 1982; Gies & Bolton 1986b; Miller et al. 2005; Hanke et al. 2009), a scenario that likely provides a natural explanation for all of these results (see Figure 3 in Miller et al. 2005 for a suggested geometry).

A potential alternative origin for the absorption could be that this arises in a disk wind, similar to those seen in the soft states of other Galactic BHBs (e.g., Miller et al. 2006). However, we do not consider this to be all that likely. The orbital modulation indicated in Figure 10 would not be expected in this scenario (although with so few data points it is difficult to completely exclude a coincidental alignment of the orbital phase and the strength of any disk wind). Furthermore, this absorption is also seen in the hard state (Parker et al. 2015; Miškovičová et al. 2016), which is not typical of other BHB systems that exhibit absorption from soft state disk winds (e.g., Neilsen & Lee 2009). In particular, using *Chandra* HETG observations, Miškovičová et al. (2016) find evidence for a similar orbital variation to that observed here in the ionized phase of the absorption seen during a hard state. Finally, regardless of whether the orbital inclination (~27°) or the inner disk inclination (~40°) should be considered here, disk winds are not seen in X-ray binary systems viewed at similarly low inclinations, even when they are in the soft state (Ponti et al. 2012).

Finally, we also see some level of variability in the flux of the narrow core of the iron emission. This also shows some evidence for an orbital modulation (see Figure 10, right panel), although this is much more marginal than for the ionized absorption, being driven solely by epoch 4. Nevertheless, the evolution is broadly consistent with the modulation expected should the narrow core arise through reprocessing of the X-ray emission within the stellar wind, or even on the stellar surface facing the black hole, because the body of the stellar companion would block at least some of the line emitting region away from superior conjunection in both cases.

From our observation closest to $\phi_{\rm orb} = 0.5$, we measure an equivalent width of 10 ± 5 eV for the narrow emission (see Table 2). For neutral iron, and the illuminating spectrum observed ($\Gamma \sim 2.6$), reprocessing by material with solar abundances subtending a solid angle of 2π should give an equivalent width of ~100 eV (George & Fabian 1991). Correcting for the projected area of the companion, given the stellar radius of ~16.5 $R_\odot$, the orbital separation of ~40 $R_\odot$, and the orbital inclination of ~27° (Hanke et al. 2009; Orosz et al. 2011), as well as the super-solar abundance inferred here, we estimate an equivalent width of ~20 eV would be expected from the stellar surface, if uniformly illuminated. This is slightly larger than observed. However, we stress that this should be considered an upper limit, because the accretion disk around Cygnus X-1 must provide some shadowing of the stellar surface. Given the warp in the disk inferred here, this effect is not trivial to estimate. Furthermore, some line emission from the stellar wind from which Cygnus X-1 accretes must also be present. Torrejón et al. (2010) find that the narrow line emission from HMXBs taken as an ensemble is consistent with a roughly spherically distributed reprocessor around the X-ray source, as expected for the stellar wind. Watanabe et al. (2006) find that the iron emission from the neutron star HMXB Vela X-1 requires contributions from both the stellar wind and the stellar photosphere. It is possible that the narrow line emission observed from Cygnus X-1 is a similar blend of the two, but we

are not able to make any firm separation of their contributions based on the data considered here.

5. CONCLUSIONS

We have undertaken a multi-epoch analysis of soft state observations of Cygnus X-1 with *NuSTAR* to investigate the spectral variability observed during this state. Our detailed modeling, using self-consistent reflection models to account for reprocessing of the primary X-ray emission by the accretion disk, finds excellent consistency across all epochs for the black hole spin, and the iron abundance of the disk, quantities that should not vary on observational timescales. We confirm that Cygnus X-1 hosts a rapidly rotating black hole, finding $0.93 \lesssim a^* \lesssim 0.96$. This is in broad agreement with the majority of prior studies of the relativistic disk reflection and also with constraints on the spin obtained through studies of the thermal accretion disk continuum. The iron abundance obtained is super-solar (Fe/solar $\sim$ 4) and in qualitative agreement with previous studies.

Our work also confirms the apparent misalignment between the inner disk and the orbital plane of the binary system reported previously. We find that the magnitude of this warp is $\sim 10^\circ$–15°($i_{\rm orb} \sim 27^\circ$, and we find $i_{\rm disk} \sim 40^\circ$), and that the level of misalignment does not appear to vary significantly with time or accretion state. This does not significantly change, and may even improve, the agreement between the reflection results presented here and the thermal continuum results regarding the black hole spin.

The spectral variability observed by *NuSTAR* is dominated by variations in the primary continuum. We find evidence that the temperature of the scattering electron plasma changes from epoch to epoch, causing the variations observed in the spectrum at the highest energies probed by *NuSTAR*. Finally, all epochs show absorption from ionized iron at $\sim$6.7 keV. The strength of this absorption varies across the orbital phase of Cygnus X-1 in a manner consistent with the absorbing material being an ionized phase of the focused stellar wind from its supergiant companion.

The authors would like to thank the referee for prompt and useful feedback. DB acknowledges financial support from the French Space Agency (CNES). VG acknowledges financial support provided by NASA through the Smithsonian Astrophysical Observatory (SAO) contract SV3-73016 to MIT for Support of the *Chandra* X-Ray Center (CXC) and Science Instruments; CXC is operated by SAO for and on behalf of NASA under contract NAS8-03060. This research made use of data obtained with *NuSTAR*, a project led by Caltech, funded by NASA, and managed by NASA/JPL, and has utilized the NUSTARDAS software package, jointly developed by the ASI Science Data Center (ASDC, Italy) and Caltech (USA). *Swift* BAT transient monitor results are provided by the *Swift* BAT team. This research has also made use of *MAXI* data provided by RIKEN, JAXA, and the *MAXI* team.

Facility: NuSTAR.

APPENDIX
NuSTAR SPACECRAFT SCIENCE (MODE 6) DATA REDUCTION

For the *NuSTAR* mission, "spacecraft science" (mode 6) events refer to those collected during periods in which an aspect solution is not available from the on board star tracker located on the X-ray optics bench (Camera Head Unit 4, or CHU4, which is the primary method for determining the absolute pointing; see Harrison et al. 2013). When CHU4 is not available, because it is either blinded by a bright target or Earth-occultation, the aspect reconstruction (source sky coordinate calculation) is calculated using the spacecraft bus attitude solution. In normal operations when the aspect reconstruction uses CHU4 to calculate source coordinates, the accuracy is $\pm 8''$. Using the spacecraft bus in mode 6, this error increases to $\sim 2'$.

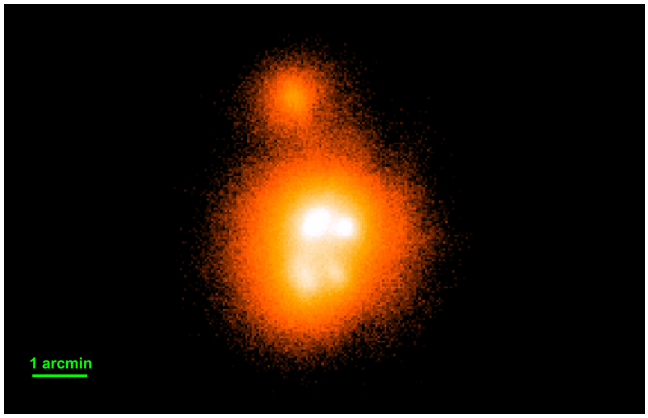

Figure 11. Sky image extracted from the full FPMA spacecraft science (mode 6) event file for one of the *NuSTAR* observations of Cygnus X-1 (OBSID 10002003001). Owing to the switching between different CHU combinations, multiple centroids from the same source can be observed. In this extreme case, five centroids are seen.

The inaccuracies incurred from the spacecraft bus attitude solution come about due to thermal flexure in the mounting of the spacecraft bus star cameras (CHU1, 2, 3), which are unique for each pointing and cannot be modeled. They manifest themselves in the calculated source coordinates, which can cause the sky image of the source to appear with multiple centroids as shown in Figure 11. There are a total of three star tracker CHUs on the spacecraft bus with a total of seven different combinations. Each one of those combinations will have a unique offset and a typical observation has between 2 and 5 of such CHU combinations. The severity of the offsets is dependent on the Solar aspect angle and some unknown variables that make them unpredictable. As such, mode 6 data is *not* recommended for applications in which imaging capability is necessary.

Because all responses are calculated in the optics frame, whose relation to the detector plane is accurately tracked by a laser system, the spectrum of the source remains unaffected by mode 6. The only problem with using mode 6 is the degradation of the PSF and the challenges with choosing the correct spectral extraction regions, because the optimal region for one CHU combination will not be the optimal region for another CHU combination. Effective areas will be calculated for the center of a region, which means that if a centroid is far outside the region it will be assigned the wrong effective area.

For sources with concentrated centroids (differences of $<1'$), simply choosing a large region is sufficient. If the source centroids are scattered (difference $>1'$) then it will be necessary to divide the observation into periods that correspond to the individual CHU combinations present during the observation and extract the spectra from these periods separately. This can

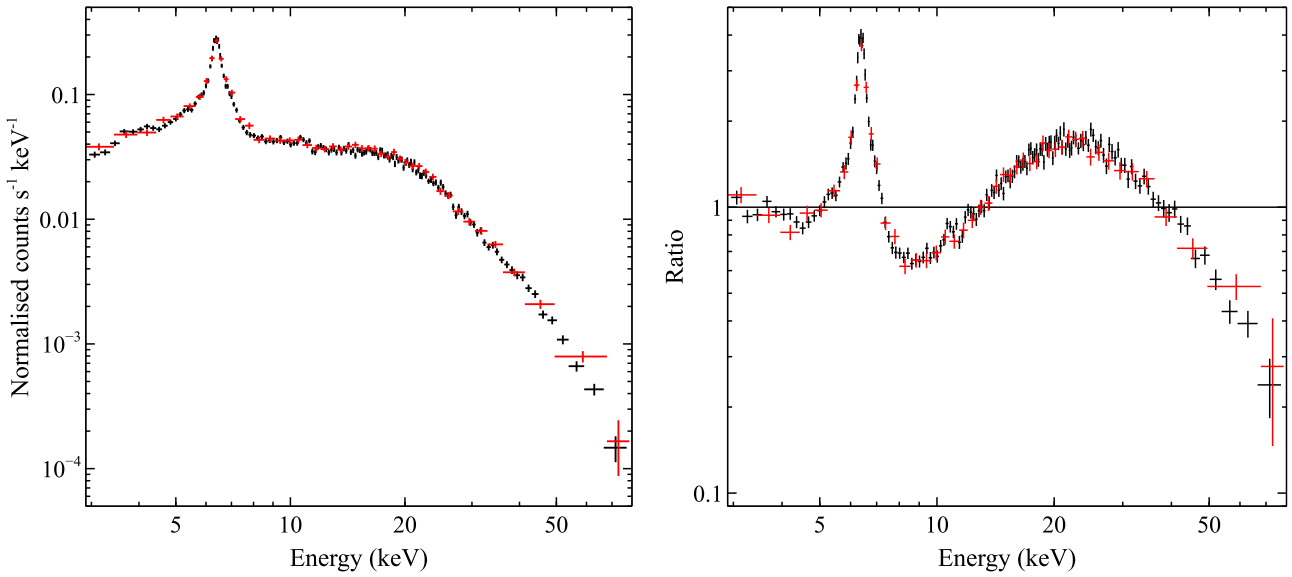

Figure 12. Spectra extracted from the targeted *NuSTAR* observation of the Circinus galaxy nucleus (OBSID 60002039002). The regular science data (mode 1) are shown in black, and the spacecraft science data (mode 6) are shown in red; only FPMA data are shown for clarity. We plot both the count spectrum (left panel) and a data/model ratio to a power-law model (right panel). Excellent agreement is seen between the two spectra, as expected given the lack of variability observed from this source (Arévalo et al. 2014).

be done by filtering on the housekeeping file `hk/xx_chu123.fits` for the different CHU combinations. The file contains the attitude solutions from the three spacecraft bus star trackers CHU1, CHU2, and CHU3. There is an extension for each CHU and the `VALID` column marks whether the CHU was active (1 = on, 0 = off). In addition, the columns `RESIDUAL`, `STARSFAIL`, `OBJECTS`, and `QCHU[3]` should be included in the filtering. A particular CHU was active if:

1. `VALID` = 1
2. `RESIDUAL` < 20
3. `STARSFAIL` < `OBJECTS`
4. `QCHU[3]` ≠ 1.

Here, `RESIDUAL` is a residual of the aspect solution fit, `OBJECTS` is the number of point sources detected by the star trackers, `STARSFAIL` is the number of these objects without known stellar counterparts in the reference catalog used (which is based on the *Hipparcos* and Tycho-2 catalogs; Perryman et al. 1997; Høg et al. 2000), and `QCHU[3]` is the real part of the position quaternion solution for the spacecraft orientation, which must be `QCHU[3]` ≠ 1 for a valid solution. As mentioned above, there are seven possible combinations: CHU1 only, CHU2 only, CHU3 only, CHU1&2, CHU1&3, CHU2&3, and CHU1&2&3. Generating GTIs for each combination will separate the centroids in time. There may still be weak centroids remaining from other CHU combinations that come from spurious solutions interspaced with the primary CHU combination the data are filtered on. This is in part because not all solutions are telemetered to the ground, and switches between CHU combinations could happen in between. Should this prove to be the case, source regions should be selected to include all the counts from each of these centroids, such that the PSF correction applied by the pipeline will be as accurate as possible.

After spectra have been extracted for each CHU combination, they can be combined as standard with tools like ADDASCASPEC. ARFs must be generated and combined for each CHU combination, but new RMFs do not necessarily need to be generated if all the events fall on the same detector as the regular (mode 1) data.

In order to demonstrate the reliability of the mode 6 data, we show in Figure 12 a comparison of the spectra extracted from modes 1 and 6 for the nucleus of the Circinus galaxy. This is a bright source that is unresolved by *NuSTAR*, and as a Compton-thick AGN is known to exhibit a stable flux. We therefore expect good agreement between the two extractions. A full scientific analysis of this source is presented in Arévalo et al. (2014). For brevity we use only the data from OBSID 60002039002, in which the nucleus was on-axis as the primary target; we do not consider the additional *NuSTAR* observations of the Circinus galaxy, which were centered on the nearby ultraluminous X-ray source (ULX; Walton et al. 2013a).

The mode 1 data are reduced following standard procedure (see Section 2), with source spectra extracted from a circular region of radius 100″, and the background was estimated from a nearby region on the same detector, avoiding the ULX. The mode 6 data was reduced following the procedure outlined above. Two centroids can be seen in the mode 6 image, but one dominates and the offset of the other is not very large, so we extract source spectra from a single, slightly larger circular region of radius 110″, which incorporates both; background was estimated in the same manner as for mode 1. The good mode 1 exposure for this observation is ∼54 ks, and the good mode 6 exposure is ∼12 ks. As can be seen from Figure 12, the two spectra of the nucleus agree well, and the fluxes returned for the two modes are consistent to within 2% for both FPMA and FPMB.

REFERENCES

Arévalo, P., Bauer, F. E., Puccetti, S., et al. 2014, ApJ, 791, 81
Arnaud, K. A. 1996, in ASP Conf. Ser. 101, Astronomical Data Analysis Software and Systems V, ed. G. H. Jacoby & J. Barnes (San Francisco, CA: ASP), 17
Barthelmy, S. D., Barbier, L. M., Cummings, J. R., et al. 2005, SSRv, 120, 143
Brenneman, L. W., & Reynolds, C. S. 2006, ApJ, 652, 1028
Churazov, E., Gilfanov, M., & Revnivtsev, M. 2001, MNRAS, 321, 759

Dauser, T., Wilms, J., Reynolds, C. S., & Brenneman, L. W. 2010, MNRAS, 409, 1534
Duro, R., Dauser, T., Grinberg, V., et al. 2016, arXiv:1602.08756
Duro, R., Dauser, T., Wilms, J., et al. 2011, A&A, 533, L3
Fabian, A. C., Lohfink, A., Kara, E., et al. 2015, MNRAS, 451, 4375
Fabian, A. C., Parker, M. L., Wilkins, D. R., et al. 2014, MNRAS, 439, 2307
Fabian, A. C., Rees, M. J., Stella, L., & White, N. E. 1989, MNRAS, 238, 729
Fabian, A. C., Wilkins, D. R., Miller, J. M., et al. 2012, MNRAS, 424, 217
Fender, R. P., Belloni, T. M., & Gallo, E. 2004, MNRAS, 355, 1105
Fragos, T., Tremmel, M., Rantsiou, E., & Belczynski, K. 2010, ApJL, 719, L79
Friend, D. B., & Castor, J. I. 1982, ApJ, 261, 293
Fürst, F., Müller, C., Madsen, K. K., et al. 2016, ApJ, 819, 150
Fürst, F., Nowak, M. A., Tomsick, J. A., et al. 2015, ApJ, 808, 122
García, J., Dauser, T., Lohfink, A., et al. 2014, ApJ, 782, 76
García, J., Dauser, T., Reynolds, C. S., et al. 2013, ApJ, 768, 146
García, J., & Kallman, T. R. 2010, ApJ, 718, 695
García, J. A., Dauser, T., Steiner, J. F., et al. 2015, ApJL, 808, L37
George, I. M., & Fabian, A. C. 1991, MNRAS, 249, 352
Gies, D. R., & Bolton, C. T. 1986a, ApJ, 304, 371
Gies, D. R., & Bolton, C. T. 1986b, ApJ, 304, 389
Gies, D. R., Bolton, C. T., Blake, R. M., et al. 2008, ApJ, 678, 1237
Gou, L., McClintock, J. E., Reid, M. J., et al. 2011, ApJ, 742, 85
Gou, L., McClintock, J. E., Remillard, R. A., et al. 2014, ApJ, 790, 29
Grevesse, N., & Sauval, A. J. 1998, SSRv, 85, 161
Grinberg, V., Hell, N., Pottschmidt, K., et al. 2013, A&A, 554, A88
Grinberg, V., Leutenegger, M. A., Hell, N., et al. 2015, A&A, 576, A117
Haardt, F., & Maraschi, L. 1991, ApJL, 380, L51
Hanke, M., Wilms, J., Nowak, M. A., et al. 2009, ApJ, 690, 330
Harrison, F. A., Craig, W. W., Christensen, F. E., et al. 2013, ApJ, 770, 103
Høg, E., Fabricius, C., Makarov, V. V., et al. 2000, A&A, 355, L27
Jourdain, E., Roques, J. P., & Chauvin, M. 2014, ApJ, 789, 26
Kallman, T., & Bautista, M. 2001, ApJS, 133, 221
King, A. L., Walton, D. J., Miller, J. M., et al. 2014, ApJL, 784, L2
Laming, J. M. 2015, LRSP, 12, 2
Laor, A. 1991, ApJ, 376, 90
Laurent, P., Rodriguez, J., Wilms, J., et al. 2011, Sci, 332, 438
Madsen, K. K., Harrison, F. A., Markwardt, C. B., et al. 2015, ApJS, 220, 8
Markoff, S., Nowak, M. A., & Wilms, J. 2005, ApJ, 635, 1203
Matsuoka, M., Kawasaki, K., Ueno, S., et al. 2009, PASJ, 61, 999
McClintock, J. E., Shafee, R., Narayan, R., et al. 2006, ApJ, 652, 518
McConnell, M. L., Zdziarski, A. A., Bennett, K., et al. 2002, ApJ, 572, 984
Miller, J. M., Fabian, A. C., Wijnands, R., et al. 2002, ApJ, 578, 348
Miller, J. M., Parker, M. L., Fuerst, F., et al. 2013, ApJL, 775, L45
Miller, J. M., Pooley, G. G., Fabian, A. C., et al. 2012, ApJ, 757, 11
Miller, J. M., Raymond, J., Fabian, A., et al. 2006, Natur, 441, 953
Miller, J. M., Wojdowski, P., Schulz, N. S., et al. 2005, ApJ, 620, 398
Miškovičová, I., Hell, N., Hanke, M., et al. 2016, arXiv:1604.00364
Mitsuda, K., Inoue, H., Koyama, K., et al. 1984, PASJ, 36, 741
Morrison, R., & McCammon, D. 1983, ApJ, 270, 119
Murdin, P., & Webster, B. L. 1971, Natur, 233, 110
Natalucci, L., Tomsick, J. A., Bazzano, A., et al. 2014, ApJ, 780, 63
Nealon, R., Price, D. J., & Nixon, C. J. 2015, MNRAS, 448, 1526
Neilsen, J., & Lee, J. C. 2009, Natur, 458, 481
Nowak, M. A., Hanke, M., Trowbridge, S. N., et al. 2011, ApJ, 728, 13
Orosz, J. A., McClintock, J. E., Aufdenberg, J. P., et al. 2011, ApJ, 742, 84
Parker, M. L., Tomsick, J. A., Kennea, J. A., et al. 2016, ApJL, 821, L6
Parker, M. L., Tomsick, J. A., Miller, J. M., et al. 2015, ApJ, 808, 9
Perryman, M. A. C., Lindegren, L., Kovalevsky, J., et al. 1997, A&A, 323, 49
Ponti, G., Fender, R. P., Begelman, M. C., et al. 2012, MNRAS, 422, L11
Pozdnyakov, L. A., Sobol, I. M., & Syunyaev, R. A. 1983, ASPRv, 2, 189
Reid, M. J., McClintock, J. E., Narayan, R., et al. 2011, ApJ, 742, 83
Reis, R. C., Fabian, A. C., & Miller, J. M. 2010, MNRAS, 402, 836
Reis, R. C., Miller, J. M., Reynolds, M. T., et al. 2013, ApJ, 763, 48
Remillard, R. A., & McClintock, J. E. 2006, ARA&A, 44, 49
Reynolds, C. S. 2014, SSRv, 183, 277
Reynolds, C. S., & Begelman, M. C. 1997, ApJ, 488, 109
Rodriguez, J., Grinberg, V., Laurent, P., et al. 2015, ApJ, 807, 17
Ross, R. R., & Fabian, A. C. 2005, MNRAS, 358, 211
Ross, R. R., & Fabian, A. C. 2007, MNRAS, 381, 1697
Takahashi, T., Mitsuda, K., Kelley, R., et al. 2012, Proc. SPIE, 8443, 84431Z
Tananbaum, H., Gursky, H., Kellogg, E. M., et al. 1972, ApJL, 174, L143
Tao, L., Tomsick, J. A., Walton, D. J., et al. 2015, ApJ, 811, 51
Tomsick, J. A., Nowak, M. A., Parker, M., et al. 2014, ApJ, 780, 78
Torrejón, J. M., Schulz, N. S., Nowak, M. A., & Kallman, T. R. 2010, ApJ, 715, 947
Verner, D. A., Ferland, G. J., Korista, K. T., & Yakovlev, D. G. 1996, ApJ, 465, 487
Walborn, N. R. 1973, ApJL, 179, L123
Walton, D. J., Fuerst, F., Harrison, F., et al. 2013a, ApJ, 779, 148
Walton, D. J., Nardini, E., Fabian, A. C., Gallo, L. C., & Reis, R. C. 2013b, MNRAS, 428, 2901
Walton, D. J., Reis, R. C., Cackett, E. M., Fabian, A. C., & Miller, J. M. 2012, MNRAS, 422, 2510
Walton, D. J., Risaliti, G., Harrison, F. A., et al. 2014, ApJ, 788, 76
Watanabe, S., Sako, M., Ishida, M., et al. 2006, ApJ, 651, 421
Wik, D. R., Hornstrup, A., Molendi, S., et al. 2014, ApJ, 792, 48
Wilkins, D. R., & Fabian, A. C. 2012, MNRAS, 424, 1284
Wilms, J., Allen, A., & McCray, R. 2000, ApJ, 542, 914
Zdziarski, A. A., Lubiński, P., Gilfanov, M., & Revnivtsev, M. 2003, MNRAS, 342, 355